



Synergistic effect of Fe and BiOCl in enhancing electrocatalytic performance for oxygen evolution reaction

Vaibhav Lokhande^a, Daehan Youn^b, Dhanaji Malavekar^c, Taeksoo Ji^{a,b,*}

^a Department of Electronics Engineering, Chonnam National University, Gwangju, 61186, South Korea

^b Department of ICT Convergence System Engineering, Chonnam National University, Gwangju, 61186, South Korea

^c Optoelectronic Convergence Research Center, Department of Materials Science and Engineering, Chonnam National University, Gwangju, 61186, South Korea

ARTICLE INFO

Keywords:

OER
Water splitting
Mott-Schottky
Tafel
Overpotential
Bismuth
Iron
Dopant

ABSTRACT

Fe was added to bismuth oxychloride (BiOCl) to improve its oxygen evolution reaction(OER) catalytic activity. X-ray diffraction (XRD), field emission scanning electron microscopy (FE-SEM), EDS, and X-ray photoelectron spectroscopy (XPS) were used to analyze the material that was produced. Many electrochemical techniques, including linear sweep voltammetry (LSV), Mott Schottky, and electrochemical impedance spectroscopy (EIS), were used to conduct the electrochemical studies of Fe doped BiOCl. Fe doped BiOCl exhibited enhanced catalytic performance compared to pristine BiOCl. The best performance was observed for 0.75 M Fe doped BiOCl sample. It recorded lowest overpotential of 354 mV @ 10 mA cm⁻² and Tafel slope of 167 mV dec⁻¹. The synergistic effect of Fe doping from structural, chemical and catalytic perspective has been analyzed and presented.

1. Introduction

Rise in demand for clean energy, as well as climate change, calls for highly efficient electrochemical energy conversion and storage technologies. Renewable energy is abundant and easily accessible but it tends to be intermittent and unreliable. Total reliance on renewable energy for all our energy demands would seem impossible unless we can harness copious amounts of energy when available and store it for usage during downtime [1,2]. One way is to use the renewable energy to split water into hydrogen and oxygen and store it. The stored hydrogen is oxidized in fuel cells to release energy. This overall process from harvesting renewable energy to burning hydrogen in fuel cells is carbon neutral and extremely clean, which does not take its toll on environment [3,4].

Under basic conditions, the hydrogen evolution reaction (HER) and oxygen evolution reaction (OER) proceed according to the equations (1) and (2) given below.



OER takes place because of a mechanism that involves the transfer of four electrons. This process slows down the kinetics, which is the primary reason for the reduced efficiency [5]. Precious metal oxides, such as those based on ruthenium and iridium, are ideal OER

* Corresponding author. Department of Electronics Engineering, Chonnam National University, Gwangju, 61186, South Korea.
E-mail address: tji@chonnam.ac.kr (T. Ji).

electrocatalysts because of their ability to lower the thermodynamic barrier [6]. The limited availability and expensive cost of these catalysts, on the other hand, prevents their widespread use. Transition metal oxides, sulfides, selenides, phosphides, and nitrides have emerged as potential candidates as non-noble metal electrocatalysts for electrolysis of water [7–10].

The p-block element-based oxides make up a special kind of catalysts. These materials have suitable bandgap and oxidation states that make them excellent electrode material for photocatalysis [11,12]. Bi₂O₃ stands out among them as most suitable choice for usage on a broad scale. This is mostly due to its abundant reserves, low cost and low toxicity compared to other p-block oxides [13,14]. It has been widely reported as an excellent material for H₂ generation, CO₂ reduction and dye degradation. The OER reactivity of bismuth oxide is moderate. Therefore, it has not gained prominence. Fast electron transport and oxygen atom exchange at the heterogeneous electrode surface often underpin the electrocatalytic OER. Bi₂O₃'s semi-metallic composition restricts such charge transfer, which in turn reduces the electrocatalytic OER efficacy [15]. The rationale for improving performance would be to overcome the aforementioned challenges. Bismuth oxychloride (BiOCl) is a significant ternary photocatalytic compound. The presence of oxygen vacancies in BiOCl is associated with significant activation of oxygen molecules, as well as enhanced performance in water splitting and CO₂ reduction processes. An appropriate quantity of oxygen vacancies does, in fact, play a favorable effect in the OER activity of transition metal oxides by dramatically altering bulk (such as energy level, conductivity) and surface (such as molecular adsorption) characteristics of materials [6]. There have been few studies on the electrocatalytic performance and investigation of BiOCl, and even fewer on OER activity. Xu et al. showcases the successful synthesis of ultrathin nanosheets composed of bismuth (Bi NSs) that exhibit active nitrogen reduction reaction (NRR) capabilities. This synthesis was achieved by an in situ electrochemical reduction-assisted exfoliation technique, employing bismuth oxychloride nanoplates (BiOCl NPs) as the precursor material. The material demonstrates effective electrocatalytic activity for NRR in a 0.1 M Na₂SO₄ solution, resulting in a substantial faradaic efficiency of 14.14 % and NH₃ yield of (11.11 μg h⁻¹ mg_{cat.}⁻¹) at -0.5 V (vs. R.H.E) and a notable NH₃ selectivity [16]. Shao et al. conducted a hydrothermal process followed by carbonization and etching conversion procedures to build heterostructures of N-doped and carbon encapsulated BiOCl-CNTs. The enhanced catalyst exhibits a significantly elevated half-wave potential (E_{1/2}) of 0.85 V (against reversible hydrogen electrode), a substantial limiting current density of -5.34 mA cm⁻² at 0.6 V in an alkaline environment, and nearly perfect 4e-reduction capabilities, surpassing those of traditional Pt/C catalysts [17]. Thirumalraj et al. used a green synthesis approach to create a hetero-junction composite of BiOCl/BiVO₄@GO and used its superior electrocatalytic activity for Promethazine hydrochloride (PMZ) detection and real-time analysis of PMZ in urine samples [18]. Miao Lv et al. report the fabrication of BiOCl/sulfonated graphene composite microspheres through hydrothermal method and employed plasma modification for creating adequate oxygen vacancies for efficient OER. The overpotential of the OER exhibited a reduction from 766 mV to 496 mV, while the Tafel slope experienced a decrease from 162 mV dec⁻¹ to 52 mV dec⁻¹ [19].

In this study, a novel and effective catalyst for the oxygen evolution reaction (OER) was synthesized and characterized. The catalyst, Bismuth oxychloride (BiOCl), was found to exhibit great efficiency despite not containing any noble metals. Fe was added to it to increase the catalytic activity of OER [20,21]. The material synthesized was characterized by X-ray diffraction (XRD), field emission scanning electron microscopy (FE-SEM), EDS and, X-ray photoelectron spectroscopy (XPS). Several electrochemical techniques, including linear sweep voltammetry (LSV), Mott Schottky, and electrochemical impedance spectroscopy (EIS), were used to conduct the electrochemical studies of Fe doped BiOCl.

2. Experimental

2.1. Materials

Bismuth (III) Chloride (BiCl₃, Sigma Aldrich), Ferrous Chloride tetrahydrate (FeCl₂·4H₂O, Sigma Aldrich), were used as precursors. 1 M KOH solution was used to adjust the pH of the solution.

2.2. Synthesis of BiOCl and Fe doped BiOCl

Bismuth (III) Chloride (BiCl₃) 1 M was dissolved in a 75 ml deionized water (DI) under constant stirring. The solution was sealed in an autoclave after being transferred to a 100 ml Teflon liner. The autoclave was heated in an oven for 12 h at 200 °C before being allowed to cool naturally. The powder was retrieved and washed three times with ethanol and deionized water. BiOCl powder was dried by heating it at 80 °C overnight in a vacuum oven. The sample was later air annealed at 650 °C for 2 h. Fe doped BiOCl samples were prepared with the same procedure as BiOCl. 0.5, 0.75 and 1 M FeCl₂ was added to the bismuth precursor solution to get Fe doped BiOCl samples.

The electrodes were fabricated using slurry cast method on to Ni foam (1*1 cm). The as prepared powders (100 mg) were mixed with PVDF, Carbon black and Nafion solution to make a slurry. The slurry was painted on to the Ni foam and dried at 180 °C to remove all the Nafion. The electrodes prepared will henceforth be denoted as 'xFe-BiOCl', where x stands for the Fe precursor's molar concentration.

2.3. Characterization of materials

For XRD measurement, the sample powder precipitate was gathered. The Bruker AXS D8 Advance Model was used to perform the X-ray diffraction analysis (XRD) utilizing copper radiation (K with = 1.54 Å). At a scanning rate of 4°/s, the XRD spectra were captured for 2θ values ranging from 10° to 90°. The surface morphology was examined using a field emission scanning electron microscope (FE

SEM, Model: JSM 6700F, Japan). VG Multilab 2000 was used to conduct X-ray photoelectron spectroscopy in order to ascertain the chemical composition of the surface. The Gaussian distribution approach was used to fit the XPS data.

2.4. Electrochemical measurements

Wonatech WBCS3000S and Zive SP1 were used to perform the electrochemical characterization. A three-electrode setup with Pt acting as the counter electrode in a 1 M aqueous electrolyte solution of KOH, saturated calomel electrode (SCE) as the reference electrode, and the electrodes as fabricated as the working electrodes was used to perform all electrochemical experiments. The LSV was performed at 1 mV s^{-1} scan rate in the potentials between of +0.0 V to +1.0 V versus SCE in 1 M KOH electrolyte. Using the Nernst equation (3), measured potential values were translated from the SCE scale to the reversible hydrogen electrode (RHE) scale:

$$E_{RHE} = E_{SCE} + 0.059 \text{ pH} + E_{SCE}^{\circ} \quad (3)$$

where, E_{SCE} is potential versus SCE electrode, and E_{SCE}° is standard redox potential of SCE at 298 K ($0.244 \text{ V} \pm 0.001 \text{ V}$), and E_{RHE} is the converted potential versus RHE. The LSV curve at the given current density j (mA cm^{-2}) was used to compute the electrocatalytic efficiency in terms of overpotential (η) according to equation (4):

$$\eta_j(V) = E_{RHE}(V) - 1.23 \text{ V} \quad (4)$$

Electrochemical impedance spectroscopy (EIS) provides great insights in the electrochemical behavior of the material. The EIS measurements were done at different bias potentials with alternating current (ac) perturbation of 5 mV, and within frequency range 100 KHz – 100 mHz.

3. Results and discussion

3.1. Synthesis and characterization

Fig. 1 shows the X ray diffraction pattern of the samples. BiOCl sample matched perfectly with the COD 96-900-9163. The diffraction peaks (2θ) of BiOCl at 11.95° , 24.08° , 25.8° , 32.44° , and 33.40° were indexed to the (001), (002), (101), (110), and (102) crystal facets of reference pattern (COD 96-900-9163). The tetragonal phase of BiOCl with space group P 4/n m has lattice constants $a = 3.890 \text{ \AA}$, $c = 7.369 \text{ \AA}$. The XRD patterns of Fe doped samples show great deviation from the tetragonal phase and are matched with monoclinic BiOCl (COD 96-810-4381) with lattice constants $a = 29.4400 \text{ \AA}$, $b = 3.9690$, and $c = 9.9950 \text{ \AA}$. The 0.5Fe–BiOCl, 0.75Fe–BiOCl, and 1Fe–BiOCl clearly show transition from tetragonal to monoclinic phase with none of the peaks matching with iron oxide. It is well known that the radii of the Bi^{3+} ion is 1.03, whereas the radii of the Fe^{3+} ion is 0.79. This fact may play a role in the replacement of the larger Bi^{3+} ions with the more manageable Fe^{3+} ions, and the Fe^{3+} ion may be integrated into the crystal lattice of the BiOCl compound. The XRD patterns matched to their respective reference patterns are shown in supplementary information (SI)

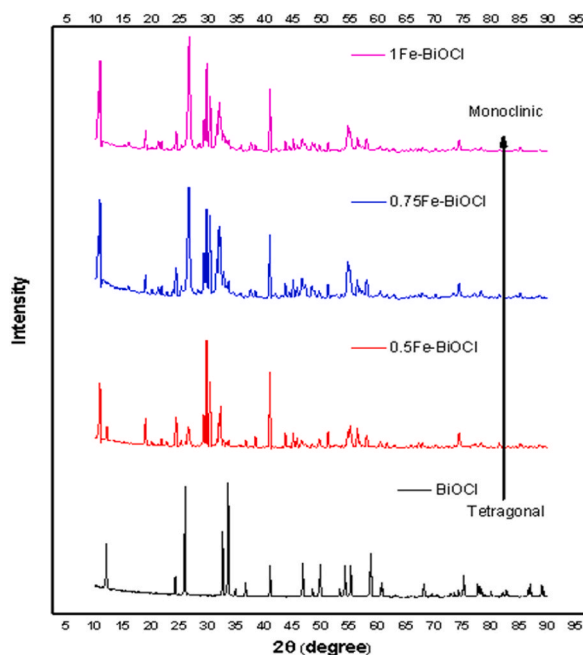


Fig. 1. XRD pattern of the as prepared samples showing transition from tetragonal to monoclinic crystal structure.

Fig. S1.

FE-SEM was used to assess the morphologies of as prepared samples. The BiOCl particles are rod shaped and similar in size as noticed in Fig. 2 (a). The shape of the Fe–BiOCl particles changes dramatically with incorporation of iron which results in complete collapse of the structure. Fig. 2 (b) shows fused plate like particles for 0.5Fe–BiOCl sample. Higher level of aggregation and fusion of the particles is observed for 0.75Fe–BiOCl as seen in Fig. 2 (c).

Interestingly for 1Fe–BiOCl, as observed in Fig. 2 (d), the particle size reduces significantly leading to granular morphology. Iron is believed to play a role in directing the crystal growth, resulting in the formation of the unique morphology. From the Fig. 2, this effect is clearly visible.

XPS analysis was done to study the valence states and presence of elements. Fig. 3 (a) shows the peaks of Bi 4f_{7/2} and Bi 4f_{5/2} for BiOCl are located at 159.53 and 164.84 eV. The spin orbital doublet splitting of 5.31 eV is observed, which indicates and confirms the presence of Bi³⁺ [22]. The Bi 4f shifts towards lower binding energy for Fe–BiOCl samples indicating increase in the electron density around Bi due to addition of Fe. The similar shift has been observed in case of O 1s and Cl, 2p Fig. 3(c), XPS spectra. The O 1s spectra of the BiOCl fitting resolved into two peaks in Fig. 3 (b) are centered at 530.22 eV and a smaller peak at 531.74 eV. However, the Fe–BiOCl samples, O 1s spectra resolves into three peaks at approximately 529, 531, and 532 eV. The peak at 529 eV is assigned to surface lattice oxygen; the remaining peaks at 531 and 532 eV represent the oxygen vacancies and surface OH group, respectively [22, 23]. The shift in the oxygen 1s peak has been attributed to the presence of oxygen vacancies or to the oxidation of the catalyst surface, which can enhance the activity of the catalyst towards OER. Fe 2p spectra for the Fe–BiOCl samples reveals presence of mixed state. Fe spectra shows a gradual shift towards higher binding energy with increase in Fe content [24]. The Fig. 4(a–d) shows the comparative spectra of Bi 4f, Fe 2p, O 1s, and Cl 2p, respectively. The fitted XPS Bi 4f, O 1s, Fe 2p and Cl 2p spectra of individual Fe doped samples are shown in SI Figs. S2–S4.

Figure S5–S8 in the SI section shows the EDX spectra of the samples. The EDX spectra confirms the presence of all the elements. Tables in figure S5–S8 show the detailed compositional analysis. As the precursor amount increases, the Fe content gradually rises in at %.

3.2. Electrochemical properties

The OER electrocatalytic activity of the as prepared samples was measured in 1 M KOH solution. The overpotential of the aforementioned systems was quantified by calculating the disparity between the thermodynamic potential of water oxidation (E_{0OH–/O2}) and the potential at which a current density of 10 mA cm^{–2} is attained for each of the examined samples. Fig. 5 (a) shows the LSV curves of the samples measured at 1 mV s^{–1}. The overpotential of the samples were calculated and depicted in Fig. 5 (b). BiOCl shows overpotential of 422 mV while after Fe doping the overpotential increases slightly before achieving its lowest value for 0.75Fe–BiOCl and again exhibiting rising trend. 0.5Fe–BiOCl, 0.75Fe–BiOCl and 1Fe–BiOCl recorded overpotential of 464, 354, and 390 mV, respectively. The distorted crystal structure and suitable amount of oxygen vacancies play a vital role in the OER activity. Fe doped samples show deviation from the original tetragonal crystal structure of BiOCl. The transition from tetragonal to monoclinic alters the bond lengths and bond strength. Fe doping changes the surface chemistry and introduces oxygen vacancies, which in this case enhances the catalyst's OER activity. This point is clearly perceivable from the XPS analysis. The direction of the shift (i.e., towards lower

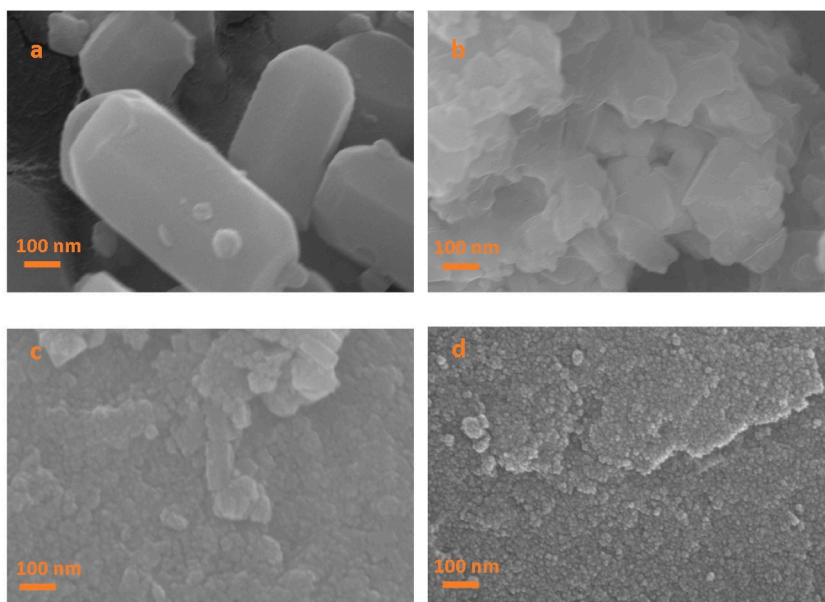


Fig. 2. SEM images of (a) BiOCl, (b) 0.5Fe–BiOCl, (c) 0.75Fe–BiOCl, and (d) 1Fe–BiOCl, respectively.

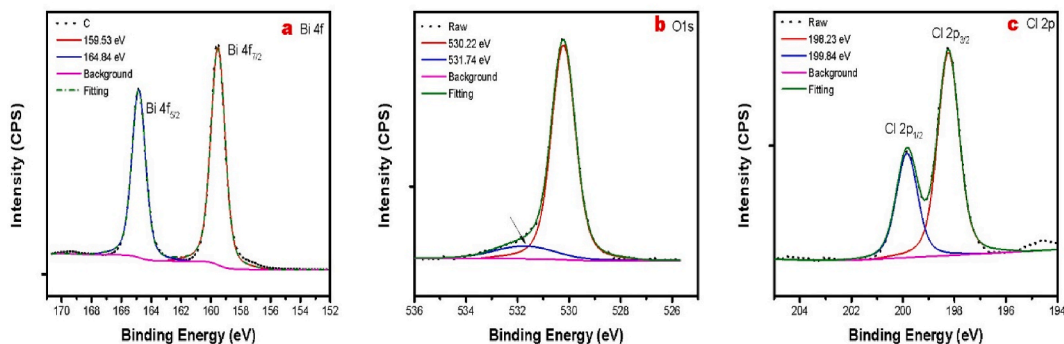


Fig. 3. XPS spectra of BiOCl sample Bi 4f (a), O (b), and Cl (c), respectively.

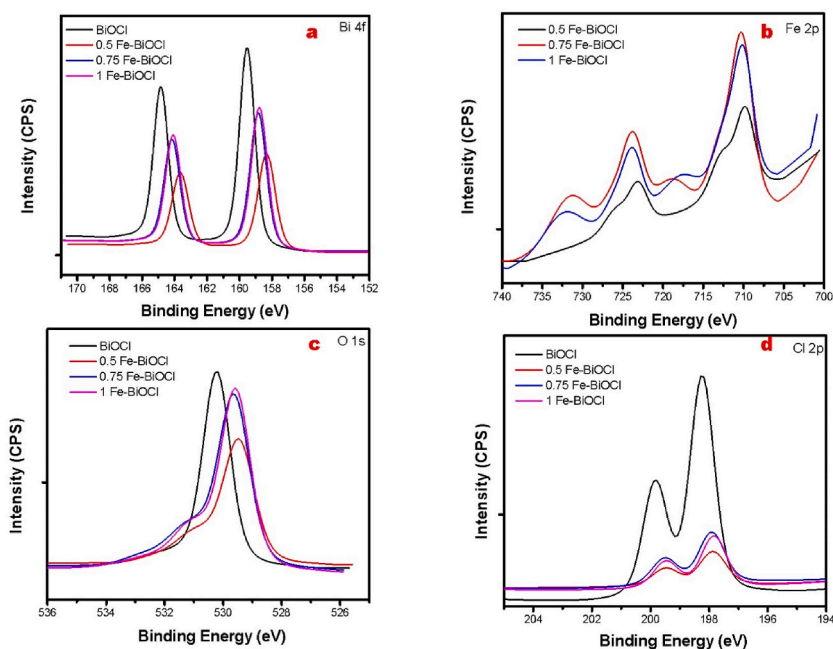


Fig. 4. Comparative XPS spectra of all samples Bi 4f (a), Fe (b), O (c), and Cl (d) respectively.

or higher binding energy levels) can provide some information about the change. In our case, the shift towards lower binding energy levels (higher energy) may indicate an increase in the electron density of the material being analyzed. This effect is observed after introducing Fe into the system, which is responsible for generating oxygen vacancies and defect in the host material. The amount of Fe incorporated into the system also has significant effect on the electrochemical performance.

Tafel curves in Fig. 5 (c) shows the trend of logarithmic current density against the applied overpotential. Tafel curve is good indicator of the electron transfer kinetics. The pristine BiOCl sample has a high Tafel slope value 390 mV dec^{-1} , which indicates the sluggish charge kinetics. However, with Fe introduction, the Tafel values improve considerably and 0.75Fe-BiOCl exhibits the lowest value 167 mV dec^{-1} amongst all the samples. In the case of 1Fe-BiOCl, the Tafel slope once again goes up, showing that the appropriate quantity of Fe concentration is necessary in order to achieve the adequate conductivity and boost the electron transfer kinetics.

Mott Schottky (MS) analysis provides a greater insight into the nature of the semiconductor, charge carrier density and the flatband potential E_{fb} . The charge carrier density, N_D , is calculated using equation (5).

$$N_D = \frac{2}{\epsilon \epsilon_0 C_0} \frac{dE}{dC} \quad (5)$$

where C is the space charge capacitance, ϵ and ϵ_0 are the permittivity of the electrode and free space, respectively, e_0 is the elementary charge, and E is the applied potential. The flat band potential, E_{fb} , is represented by the x intercept of the linear component of the MS plot. The electrode is more positively charged compared to the reference electrode when the flatband potential is higher, which implies less energy is needed to drive the OER reaction [25–28]. This may lead to a smaller OER overpotential and therefore more effective

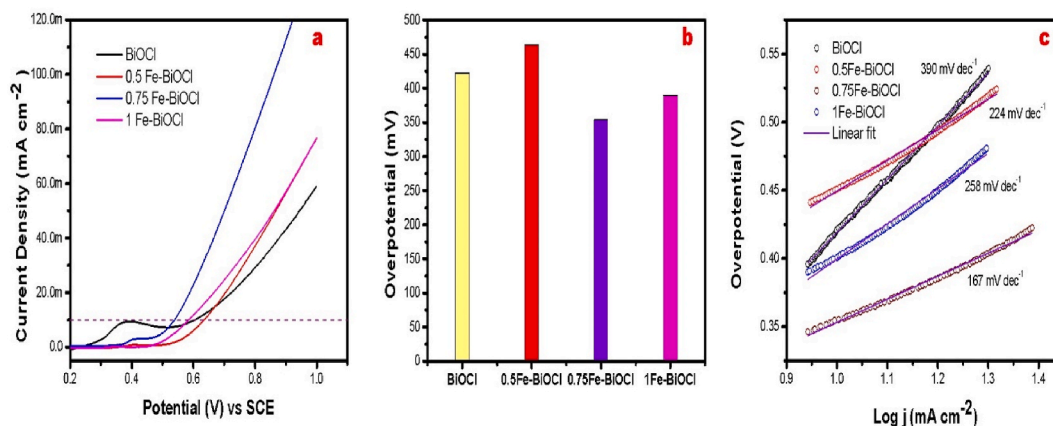


Fig. 5. LSV curve measured at 1 mVs^{-1} in 1 M KOH (a), Overpotential of the samples at 10 mA cm^{-2} (b), and Tafel curves of as prepared samples (c).

OER process. Fig. 6(a–d) shows the Mott-Schottky plot for BiOCl, 0.5Fe–BiOCl, 0.75Fe–BiOCl, and 1Fe–BiOCl, respectively and the x intercept denotes the flatband potential. From the graph the E_{fb} values, for samples BiOCl, 0.5Fe–BiOCl, 0.75Fe–BiOCl, and 1Fe–BiOCl were found to be 0.268, 0.28, 0.46, and 0.38 V, respectively. The higher E_{fb} for 0.75Fe–BiOCl correlates with the lower OER overpotential and is in agreement with the behavior of other samples. This proves that the flatband potential is an important metric. It may give some insights into the electrochemical performance.

The stability of the Fe doped samples were tested at different ($10, 25, 50, 75,$ and 100 mAcm^{-2}) current densities and are shown in Fig. 7 (a), (b), and (c). 0.75Fe–BiOCl sample shows the most stable performance of all. The samples were also subjected to 6 h stability study at fixed 25 mAcm^{-2} current density. The sample 0.5Fe–BiOCl showed a less stable performance at higher overpotential. The performance decreased by 14.28 % at the end of 6 h 0.75Fe–BiOCl sample showed 7 % decrease while the 1Fe–BiOCl showed only 2 % decrease. However, the 0.75Fe–BiOCl performance was delivered at lower overpotential as compared to 1Fe–BiOCl. Stable catalytic activity of the sample demonstrates its viability as an excellent electrocatalyst.

The Nyquist plot of the samples measured at two different bias potentials 0 V and 600 mV vs SCE are shown in Fig. 8 (a) and (b), respectively. The inset in Fig. 8 (a) shows the magnified image of the highlighted section. The inset picture clearly shows the series resistance and charge transfer resistance semicircle in high frequency region. Fitting of the experimental data is carried out using ZView EIS data analysis software and the fitted values for data in Fig. 8 (b) are shown in Table 1. Fig. 8 (b) also shows the equivalent circuit diagram. The Rs block denotes the series resistance while the two parallel block consisting of the R and Q elements represent the two curves observed in the Nyquist plot.

The two semicircles that are observed for all the samples signify the charge transfer and mass diffusion. A perfect semicircle in the low frequency range is indicative of the high double layer capacitance and efficient ion adsorption. The form of the semicircle is slightly distorted in our case, and this is true for all of the samples; this indicates restriction on the mass transfer of reactants and products. The values obtained from fitting the curve are in perfect agreement with other data. The sample 0.75 Fe–BiOCl shows lower Rs and lower charge transfer resistance (R1) than other samples. This indicates that the overpotential is effectively lowered due to lower transfer resistance.

4. Conclusion

BiOCl is an excellent photo electrode for water splitting but its performance, as an electrocatalyst for OER is moderate at best. In this work, we attempted to enhance the electrocatalytic performance of the host material by use of a dopant. The addition of Fe into BiOCl has a positive impact on the electrocatalytic performance. Fe doping into BiOCl resulted into transition of its crystal structure there by resulting into a large distorted structure. This fact was also confirmed with the help of XPS, where in the elements of the host material showed decreased electronegativity and increase in electron density while Fe exhibited the opposite trend. Doping also resulted in the higher flatband potential. The overpotential for the doped material consequently reached to its lowest value of 354 mV with Tafel slope of 167 mV dec^{-1} . The analysis of the material has prompted towards a specific trend, which can be useful while designing future OER materials. Further research is needed to completely understand the factors and their role in OER material design and synthesis.

Author contribution statement

Vaibhav Lokhande: Conceived and designed the experiments; Performed the experiments; Analyzed and interpreted the data; Contributed reagents, materials, analysis tools or data; Wrote the paper. Daehan Youn; Dhanaji Malavekar: Contributed reagents, materials, analysis tools or data. Taeksoo ji: Conceived and designed the experiments; Analyzed and interpreted the data; Wrote the

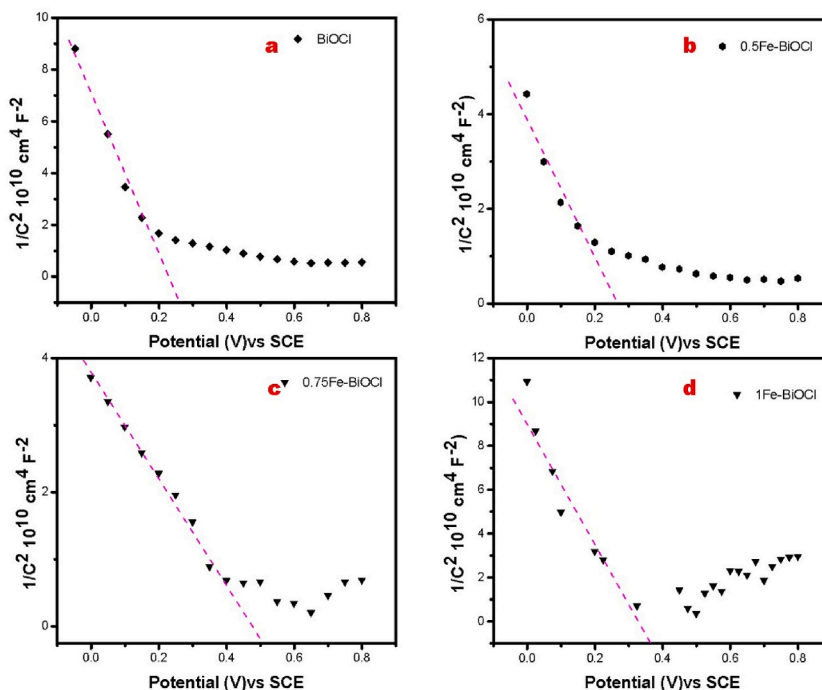


Fig. 6. Mott Schottky plot BiOCl (a), 0.5Fe-BiOCl (b), 0.75Fe-BiOCl (c), and 1Fe-BiOCl (d) and flatband potential determination.

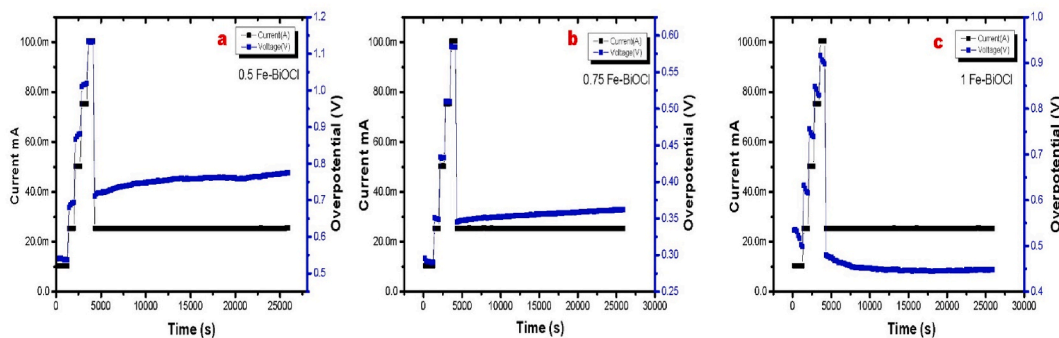


Fig. 7. Stability graph for the samples 0.5Fe-BiOCl (a), 0.75Fe-BiOCl (b), and 1Fe-BiOCl (c), respectively.

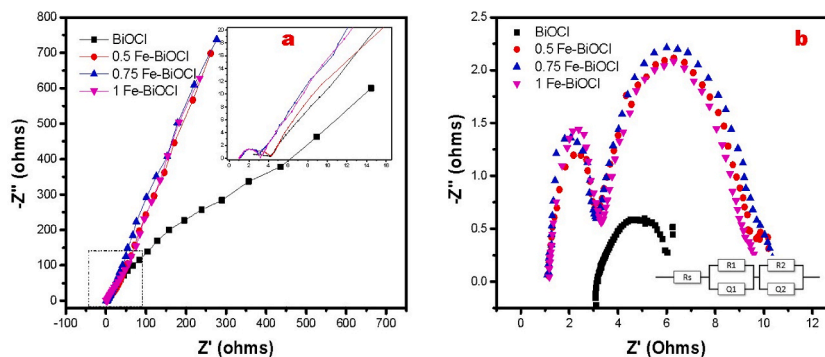


Fig. 8. Nyquist plot of samples at (a) 0 V and (b) at 600 mV vs S-C.E bias.

Table 1

Values of EIS parameters obtained after fitting the curve.

Sample	Rs(Ω cm ⁻²)	R1(Ω cm ⁻²)	R2(Ω cm ⁻²)	Q1(F) y a		Q2(F) y a	
BiOCl	3.12	1.5	2.06	3.71×10^{-3}	483×10^{-3}	55×10^{-3}	479.9×10^{-3}
0.5Fe–BiOCl	1.2	7.14	1.5	6.25×10^{-3}	6.773×10^{-3}	891×10^{-9}	1.257
0.75 Fe–BiOCl	1.05	1.78	4.2	4.872	1.14	6.5×10^{-3}	705.8×10^{-3}
1 Fe–BiOCl	1.14	6.4	1.9	6.5×10^{-3}	729×10^{-3}	5.07×10^{-6}	1.1

paper.

Data availability statement

Data will be made available on request.

Declaration of competing interest

The authors declare that they have no known competing financial interests or personal relationships that could have appeared to influence the work reported in this paper.

Acknowledgements

This research was supported in part by Basic Science Research Program through the National Research Foundation of Korea (NRF) funded by the Ministry of Education under Grant NRF-2021R1F1A1049947, and by the MSIT (Ministry of Science and ICT), Korea, under the Innovative Human Resource Development for Local Intellectualization support program(IITP-2023-RS-2022-00156287) supervised by the IITP(Institute for Information & communications Technology Planning & Evaluation).

Appendix A. Supplementary data

Supplementary data to this article can be found online at <https://doi.org/10.1016/j.heliyon.2023.e20811>.

References

- [1] Y.J. Kim, A. Lim, J.M. Kim, D. Lim, K.H. Chae, E.N. Cho, H.J. Han, K.U. Jeon, M. Kim, G.H. Lee, G.R. Lee, H.S. Ahn, H.S. Park, H. Kim, J.Y. Kim, Y.S. Jung, Highly efficient oxygen evolution reaction via facile bubble transport realized by three-dimensionally stack-printed catalysts, *Nat. Commun.* 2020 111 (11) (2020) 1–11, <https://doi.org/10.1038/s41467-020-18686-0>.
- [2] V.R. Stamenkovic, B.S. Mun, M. Arenz, K.J.J. Mayrhofer, C.A. Lucas, G. Wang, P.N. Ross, N.M. Markovic, Trends in electrocatalysis on extended and nanoscale Pt-bimetallic alloy surfaces, *Nat. Mater.* 6 (2007) 241, <https://doi.org/10.1038/nmat1840>.
- [3] Hydrogen Production and Delivery | Hydrogen and Fuel Cells | Hydrogen and Fuel Cells | NREL (n.d.), <https://www.nrel.gov/hydrogen/hydrogen-production-delivery.html#publications> (accessed March 7, 2023).
- [4] Y. Gao, Y. Liu, H. Yu, D. Zou, High-entropy oxides for catalysis: status and perspectives, *Appl. Catal. Gen.* 631 (2022), 118478, <https://doi.org/10.1016/J.APCATA.2022.118478>.
- [5] C. Feng, M.B. Faheem, J. Fu, Y. Xiao, C. Li, Y. Li, Fe-based electrocatalysts for oxygen evolution reaction: progress and perspectives, *ACS Catal.* 10 (2020) 4019–4047, <https://doi.org/10.1021/ACSCATAL.9B05445>.
- [6] F. Song, L. Bai, A. Moysiadou, S. Lee, C. Hu, L. Liardet, X. Hu, Transition metal oxides as electrocatalysts for the oxygen evolution reaction in alkaline solutions: an application-inspired renaissance, *J. Am. Chem. Soc.* 140 (2018) 7748–7759.
- [7] K. Wang, X. Wang, Z. Li, B. Yang, M. Ling, X. Gao, J. Lu, Q. Shi, L. Lei, G. Wu, Y. Hou, Designing 3d dual transition metal electrocatalysts for oxygen evolution reaction in alkaline electrolyte: beyond oxides, *Nano Energy* 77 (2020), 105162, <https://doi.org/10.1016/J.NANOEN.2020.105162>.
- [8] X. Peng, Y. Yan, X. Jin, C. Huang, W. Jin, B. Gao, P.K. Chu, Recent advance and prospectives of electrocatalysts based on transition metal selenides for efficient water splitting, *Nano Energy* 78 (2020), 105234, <https://doi.org/10.1016/J.NANOEN.2020.105234>.
- [9] Y. Liu, Y. Guo, Y. Liu, Z. Wei, K. Wang, Z. Shi, A mini review on transition metal chalcogenides for electrocatalytic water splitting: bridging material design and practical application, *Energy Fuel.* 37 (2022), 10.1021/Acs.Energyfuels.2c03833/Asset/Images/Large/Ef2c03833_0009.jpeg.
- [10] A.S. Sabir, E. Pervaiz, R. Khosa, U. Sohail, An inclusive review and perspective on Cu-based materials for electrochemical water splitting, *RSC Adv.* 13 (2023) 4963–4993, <https://doi.org/10.1039/D2RA07901A>.
- [11] Z. Yang, F.E. Oropeza, K.H.L. Zhang, P-block metal-based (Sn, In, Bi, Pb) electrocatalysts for selective reduction of CO₂ to formate, *Appl. Mater.* 8 (2020), 060901, <https://doi.org/10.1063/5.0004194>.
- [12] S.A. Razeq, M.R. Popeil, L. Wangoh, J. Rana, N. Suwandaratne, J.L. Andrews, D. Fwatson, S. Banerjee, L.F.J. Piper, Designing catalysts for water splitting based on electronic structure considerations, *Electron. Struct.* 2 (2020), 023001, <https://doi.org/10.1088/2516-1075/AB7D86>.
- [13] B. Hai, C. Liu, Heterostructured Bi₂O₃@rGO anode for electrochemical sodium storage, *Mater.* 2022 15 (2022) 2787, <https://doi.org/10.3390/MA15082787>, 2787. 15.
- [14] Asha Raveendran, Mijun Chandran, Ragupathy Dhanusuraman, A comprehensive review on the electrochemical parameters and recent material development of electrochemical water splitting electrocatalysts, *RSC Adv.* 13 (2023) 3843–3876, <https://doi.org/10.1039/D2RA07642J>.
- [15] S.K.T. Aziz, M. Ummekar, I. Karajagi, S.K. Riyajuddin, K.V.R. Siddhartha, A. Saini, A. Potbhare, R.G. Chaudhary, V. Vishal, P.C. Ghosh, A. Dutta, A Janus cerium-doped bismuth oxide electrocatalyst for complete water splitting, *Cell Reports Phys. Sci.* 3 (2022), 101106, <https://doi.org/10.1016/J.XCRP.2022.101106>.
- [16] Y. Xu, T. Ren, S. Yu, H. Yu, S. Yin, Z. Wang, X. Li, L. Wang, H. Wang, In situ electrochemical reduction-assisted exfoliation: conversion of BiOCl nanoplates into Bi nanosheets enables efficient electrocatalytic nitrogen fixation, *Sustain. Energy Fuels* 4 (2020) 3334–3339, <https://doi.org/10.1039/D0SE00445F>.

- [17] X. Shao, Y. Yang, Y. Liu, P. Yan, S. Zhou, T. Taylor Isimjan, X. Yang, Oxygen vacancy-rich N-doped carbon encapsulated BiOCl-CNTs heterostructures as robust electrocatalyst synergistically promote oxygen reduction and Zn-air batteries, *J. Colloid Interface Sci.* 607 (2022) 826–835, <https://doi.org/10.1016/j.jcis.2021.08.210>.
- [18] B. Thirumalraj, D.P. Jaihindh, S.O. Alaswad, M.S.P. Sudhakaran, M. Selvaganapathy, A. Alfaantazi, H. Choe, K. Kwon, Fabricating BiOCl/BiVO₄ nanosheets wrapped in a graphene oxide heterojunction composite for detection of an antihistamine in biological samples, *Environ. Res.* 212 (2022), 113636, <https://doi.org/10.1016/j.envres.2022.113636>.
- [19] M. Lv, S. Jin, H. Wang, Y. Chen, T. Ma, K. Cui, J. Li, S. Wu, Z. Liu, Y. Guo, Z. Liu, X. Chang, X. Li, Plasma modified BiOCl/sulfonated graphene microspheres as efficient photo-compensated electrocatalysts for the oxygen evolution reaction, *Catal. Sci. Technol.* 10 (2020) 4786–4793, <https://doi.org/10.1039/D0CY00627K>.
- [20] C.F. Li, L.J. Xie, J.W. Zhao, L.F. Gu, H.B. Tang, L. Zheng, G.R. Li, Interfacial Fe–O–Ni–O–Fe bonding regulates the active Ni sites of Ni-MOFs via iron doping and decorating with FeOOH for super-efficient oxygen evolution, *Angew. Chem., Int. Ed.* 61 (2022), e202116934, <https://doi.org/10.1002/anie.202116934>.
- [21] C.F. Li, L.J. Xie, J.W. Zhao, L.F. Gu, J.Q. Wu, G.R. Li, Interfacial electronic modulation by Fe₂O₃/NiFe-LDHs heterostructures for efficient oxygen evolution at high current density, *Appl. Catal. B Environ.* 306 (2022), 121097, <https://doi.org/10.1016/j.apcatb.2022.121097>.
- [22] J. Zhang, Z. Wang, M. Fan, P. Tong, J. Sun, S. Dong, J. Sun, Ultra-light and compressible 3D BiOCl/RGO aerogel with enriched synergistic effect of adsorption and photocatalytic degradation of oxytetracycline, *J. Mater. Res. Technol.* 8 (2019) 4577–4587, <https://doi.org/10.1016/j.jmrt.2019.08.002>.
- [23] S. Kang, R.C. Pawar, Y. Pyo, V. Khare, C.S. Lee, Size-controlled BiOCl-RGO Composites Having Enhanced Photodegradative Properties, 2015, pp. 259–275, <https://doi.org/10.1080/17458080.2015.1047420>. <http://dx.doi.org/10.1080/17458080.2015.1047420>.
- [24] A. Rajan, M. Sharma, N.K. Sahu, Assessing magnetic and inductive thermal properties of various surfactants functionalised Fe₃O₄ nanoparticles for hyperthermia, *Sci. Reports* 2020 101 10 (2020) 1–15, <https://doi.org/10.1038/s41598-020-71703-6>.
- [25] S. Trasatti, Electrocatalysis in the anodic evolution of oxygen and chlorine, *Electrochim. Acta* 29 (1984) 1503–1512, [https://doi.org/10.1016/0013-4686\(84\)85004-5](https://doi.org/10.1016/0013-4686(84)85004-5).
- [26] H.A. Gasteiger, S.S. Kocha, B. Sompalli, F.T. Wagner, Activity benchmarks and requirements for Pt, Pt-alloy, and non-Pt oxygen reduction catalysts for PEMFCs, *Appl. Catal. B Environ.* 56 (2005) 9–35, <https://doi.org/10.1016/j.apcatb.2004.06.021>.
- [27] S. Koh, P. Strasser, Electrocatalysis on bimetallic surfaces: modifying catalytic reactivity for oxygen reduction by voltammetric surface dealloying, *J. Am. Chem. Soc.* 129 (2007) 12624–12625, <https://doi.org/10.1021/ja0742784>.
- [28] J. Greeley, I.E.L. Stephens, A.S. Bondarenko, T.P. Johansson, H.A. Hansen, T.F. Jaramillo, J. Rossmeisl, I. Chorkendorff, J.K. Nørskov, Alloys of platinum and early transition metals as oxygen reduction electrocatalysts, *Nat. Chem.* 2009 17 1 (2009) 552–556, <https://doi.org/10.1038/nchem.367>.